New Journal of Physics
The open access journal at the forefront of physics

Deutsche Physikalische Gesellschaft DPG IOP Institute of Physics

PAPER • OPEN ACCESS

Compact mid-infrared graphene thermopile enabled by a nanopatterning technique of electrolyte gates

To cite this article: Cheng Peng *et al* 2018 *New J. Phys.* **20** 083050

New Journal of Physics
The open access journal at the forefront of physics

Deutsche Physikalische Gesellschaft DPG
IOP Institute of Physics

Published in partnership with: Deutsche Physikalische Gesellschaft and the Institute of Physics

OPEN ACCESS

RECEIVED
9 April 2018

REVISED
13 August 2018

ACCEPTED FOR PUBLICATION
15 August 2018

PUBLISHED
31 August 2018

PAPER

Compact mid-infrared graphene thermopile enabled by a nanopatterning technique of electrolyte gates

Cheng Peng[1,7], **Sebastien Nanot**[2,3,7], **Ren-Jye Shiue**[1], **Gabriele Grosso**[1,4], **Yafang Yang**[5], **Marek Hempel**[1], **Pablo Jarillo-Herrero**[5], **Jing Kong**[1], **Frank H L Koppens**[2,6], **Dmitri K Efetov**[1,2] and **Dirk Englund**[1]

[1] Department of Electrical Engineering and Computer Science, Massachusetts Institute of Technology, Cambridge, MA 02139, United States of America
[2] ICFO-Institut de Ciencies Fotoniques, The Barcelona Institute of Science and Technology, E-08860 Castelldefels (Barcelona), Spain
[3] L2C-Laboratoire Charles Coulomb, Univ Montpellier, CNRS, Montpellier, France
[4] Photonics Initiative, Advanced Science Research Center, City University of New York, New York, NY 10031, United States of America
[5] Department of Physics, Massachusetts Institute of Technology, Cambridge, MA 02139, United States of America
[6] ICREA-Institució Catalana de Recerça i Estudis Avancats, E-08010 Barcelona, Spain
[7] Contributed equally to this work.

E-mail: englund@mit.edu

Keywords: graphene, 2D materials, nanopatterned electrolyte gates, high carrier density, mid-infrared, thermopile

Abstract

A central challenge in making two-dimensional (2D) material-based devices faster, smaller, and more efficient is to control their charge carrier density at the nanometer scale. Traditional gating techniques based on capacitive coupling through a gate dielectric cannot generate strong and uniform electric fields at this scale due to divergence of the fields in dielectrics. This field divergence limits the gating strength, boundary sharpness, and minimum feature size of local gates, precluding certain device concepts (such as plasmonics and metamaterials based on spatial charge density variation) and resulting in large device footprints. Here we present a nanopatterned electrolyte gating concept that allows locally creating excess charges by combining electrolyte gating with an ion-impenetrable e-beam-defined resist mask. Electrostatic simulations indicate high carrier density variations of $\Delta n \sim 10^{14}$ cm^{-2} across a length of only 15 nm at the mask boundaries on the surface of a 2D conductor. We implement this technique using cross-linked poly(methyl methacrylate), experimentally prove its ion-impenetrability and demonstrate e-beam patterning of the resist mask down to 30 nm half-pitch resolution. The spatial versatility enables us to demonstrate a compact mid-infrared graphene thermopile with a geometry optimized for Gaussian incident radiation. The thermopile has a small footprint despite the number of thermocouples in the device, paving the way for more compact high-speed thermal detectors and cameras.

1. Introduction

Modulation of charge carrier concentration of semiconductors lies at the heart of many electronic and optoelectronic device operation principles [1, 2]. This modulation is especially essential for two-dimensional (2D) van der Waals materials [3–10] where the free carrier density change is usually much stronger (2 orders of magnitude) compared to bulk materials and can be dynamically tuned with electrostatic gating methods. In recent years, rapidly developing device concepts and applications impose stronger and stronger requirements on the spatial resolution and highest-achievable carrier concentration of gating techniques. For example, a spatially sharp (~15 nm) *p*–*n* junction and a high carrier density contrast across the junction is the key to the realization of concepts such as tunnel diodes [11] and negative electron refractive index [12]. A strong in-plane electric field across the junction as a result of the junction sharpness facilitates electron–hole pair separation in the photovoltaic (PV) effect [13] and can thus improve the quantum efficiency of PV-based solar cells and photodetectors [14]. Many novel device concepts also rely on the ability to create metamaterials with spatial carrier density variations down to the nanometer scale, including for instance graphene with periodically doped

nanodisk or nanoribbon arrays for complete optical absorption in the visible and near-infrared [15, 16], graphene with doped waveguide, bend and resonator patterns for a plasmon-based nanophotonic network [17], and superlattices based on graphene and other 2D materials for concepts such as electron beam supercollimation [18–21]. Implementing these concepts calls for a gating method that allows for sharp *p–n* junctions with narrow depletion regions (~15 nm), a small minimum gating feature size, large carrier density contrasts (10^{14} cm^{-2}), strong in-plane electric fields ($>1 \times 10^8$ V m^{-1}), and the versatility to generate complex spatial doping profiles within a small area.

The state-of-the-art electrostatic gating technique for modulating charge carrier concentration and creating *p–n* junctions is the metal-dielectric split gate technique [22–24]. This method is based on the electric field effect [25] in which electric voltages are applied across a gate dielectric to induce extra charges on the 2D material surface. A *p–n* junction can be created by applying opposite electric potentials to the two sides of a boundary to induce charges with opposite polarities. Although this technique is convenient, several limitations restrict its use when more extreme requirements are desirable. In terms of carrier density contrast, dielectric-based gating can only induce a carrier concentration variation Δn of less than 2×10^{13} cm^{-2} for typical dielectrics such as SiO_2, HfO_2, SiN_x, and hexagonal-BN, due to a maximal applicable voltage across the dielectrics before the dielectric breakdown (molecular bond breakage and defects) [26–28]. In terms of junction sharpness, the carrier density has a slowly varying profile across the junction due to electric field divergence in dielectrics, with a characteristic length similar to the thickness of the dielectric, making it hard to create sharp junctions at nanoscale without using extremely thin (a few nanometers) dielectrics which typically have undesirable leakage and tunneling currents. Furthermore, due to wire-packaging difficulties and fabrication limitation of the electrodes, complex gating patterns and device geometries with large numbers of gating electrodes at the nanoscale is practically challenging.

In this paper we present a nanopatterned electrolytic gating concept that allows for a junction sharpness down to 15 nm and a minimum gating feature size of 30 nm. In contrast to dielectric-based gating, electrolyte gating can concentrate excess charges directly on the surface of the 2D material and reach a capacitance of $C = 3.2\ \mu$F cm^{-2} (250 times higher than a typical 300 nm SiO_2 gate) [29–31], which enables carrier density modification up to $\Delta n = 10^{14}$ cm^{-2}. Since patterning of electrolyte is challenging, a general method for local electrolyte gates at nanoscale has not been demonstrated so far. To achieve this goal we introduce a lithographical masking technique based on e-beam over-exposed poly(methyl methacrylate) (PMMA) that can screen ions in electrolyte. This e-beam patterned mask can prevent the mask-protected areas from being in contact with, and thus modulated by, the electrolyte gate. Hence this technique effectively creates lithographically-defined local electrolyte gates. Previously, masking of the contacts to create electrolyte gating channels or lateral doping profiles at micrometer scale has been shown with materials such as SU-8 and hydrogen silsesquioxane (HSQ) [32–35]. However, SU-8 is more commonly used as a photoresist for microstructure patterning. Previous works have demonstrated SU-8 as an e-beam resist for nanometer size patterning, but only for large pitch structures (~hundreds of nm) [36], which makes it unsuitable for creating nanoscale electrolyte gates. HSQ is a high resolution e-beam resist that is capable of creating sub-10nm patterns. However, no previous studies have been performed on the usage of HSQ as a mask for electrolyte at the nanoscale or investigated HSQ's impenetrability against electrolyte ions. Here we demonstrate patterning of electrolyte gates at the nanoscale. To argue that this technique can create nanometer-sharp junctions and spatial carrier density profiles with feature sizes down to tens of nanometers, we study the junction profile and provide several experimental proofs for the ion-impenetrability of the mask.

2. Methods

2.1. E-beam cross-linked PMMA

950PMMA A Resist from MicroChem (Westborough, Massachusetts, USA) is first spun on 2D material samples. Different dilution concentration and spin speeds are used to create PMMA thin films of different thicknesses according to the spin speed curves[8]. Since volatile groups (CO_2, H_2, CH_3O) and cross-linked carbon–carbon covalent bonds form during the e-beam irradiation, resultant cross-linked PMMA loses thickness compared to the original PMMA [37]. This thickness ratio was characterized to be ~0.6 using a Dektak stylus profiler. The resist is then baked on a hotplate at 180 °C for 2 min and exposed to electron beams with an energy of 125 keV at a dose of ~80 000 μC cm^{-2} (or electron beams with an energy of 30 keV at a dose of ~20 000 μC cm^{-2}). Finally, the resist is developed with a mixture of isopropyl alcohol and deionized water (3:1 mixing ratio) at the temperature of 4 °C for 2 min. The unexposed PMMA thin film is removed by acetone followed by a quick rinse in isopropyl alcohol.

[8] PMMA Data Sheet, Microchem.

2.2. Solid polymer electrolyte PEO–$LiClO_4$

Poly(ethylene oxide) (PEO) powder (average M_v 100,000), lithium perchlorate ($LiClO_4$) powder (99.99% purity) (both from Sigma Aldrich, St. Louis, Missouri, USA), and methanol are mixed in a weight ratio of 0.2:0.024:7.6. The solution is then warmed up to 60 °C and subsequently centrifuged at 14 000 rpm for 5 min to separate the long chain polymers from the liquid. The clear and transparent solution can then be spun coat or drop cast onto a sample and dried for 5 minutes before it is ready for use.

3. Results

Figure 1(a) illustrates the technique for a graphene sheet. When a voltage is applied between the electrolyte top gate and the graphene, ions in the electrolyte accumulate on the graphene surface, only in regions that are uncovered by the PMMA mask, creating an electrolyte gating pattern defined by the shape of the mask. An additional SiO_2 back gate allows weak *p* or *n* doping of the regions covered by the mask.

For an electrolyte gate voltage of 15 V, a carrier density contrast of $\Delta n \sim 10^{14}$ cm^{-2} can be created at the PMMA mask boundary across only ~15 nm, as shown in the blue curve in figure 1(c), produced by finite element simulations with COMSOL-Multiphysics [38]. Plotted in figure 1(d) in the blue curve is the calculated in-plane electric field intensity across the junction, showing a maximum magnitude as high as $E_{\text{in-plane}} = 550$ MV m^{-1} at the close vicinity of the mask boundary. The simulation assumes a Stern–Gouy–Chapman electrical double layer model [39] of the electrolyte ions and calculates the electric potential and the flux of ions under the influence of both ion diffusion due to the ionic concentration gradient and ion migration due to the electric field. This process is governed by the Poisson–Nernst–Planck equations. The discontinuity in the carrier density profile is caused by the difference in the electric permittivity between electrolyte medium and cross-linked PMMA mask ($\epsilon_{\text{PEO}} = 5$ and $\epsilon_{\text{PMMA}} \sim 20$). Additional details about the double layer model and parameters used in the simulation are in the supplementary information.

For comparison, the simulated doping contrast and the in-plane electric field are much lower in a metal-dielectric split gate, as indicated in the red curves in figures 1(c) and (d), rescaled for better visibility with a factor of 5. A carrier density contrast of at most $\Delta n = 2 \times 10^{13}$ cm^{-2} (1 order of magnitude lower than that with the electrolyte-PMMA-mask technique) across a length scale of ~100 nm is induced when a voltage of ~60 V is applied, corresponding to an in-plane electric field of $E_{\text{in-plane}} = 3 \times 10^7$ V m^{-1}. This simulation assumes a dielectric constant of 3.9 (SiO_2) and a thickness of 60 nm for the gate dielectric, and a gap of 100 nm between the two gate electrodes, which are typical values in the literature [22, 23]. The dielectric thickness and the gap width between the gate electrodes are the limiting factors for the junction sharpness. To achieve a sharpness of ~15 nm, both the dielectric and the gap width have to be similar in size too (see supplementary information). The former would result in undesirable leaking and tunneling currents and the latter is currently challenging from a fabrication standpoint.

In summary, our nanopatterned electrolyte gating technique can enable nanometer-sharp junctions, and carrier density contrast and in-plane electric field orders of magnitude higher than split metal gate structures.

To implement this electrolyte gating technique with the screening mask, the choice of material for the mask is essential and several requirements need to be met. To ensure high spatial carrier density modulation resolution, the lithographical resolution of the mask has to be high. To ensure correct junction profile results calculated, the assumptions made in the simulation have to be experimentally verified for the mask of choice, which include the mask's impenetrability to ions in the electrolyte, the straightness of the mask sidewalls, and the ability for the electrolyte to fill, wet and maintain contact with finely patterned nanostructures.

One suitable candidate for the mask is e-beam cross-linked PMMA. In addition to being a high resolution e-beam resist [40, 41], the e-beam cross-linking of this material produces a high carbon atom density material matrix that is nearly impermeable to electrolyte ions. Commonly used as a positive-tone e-beam resist, PMMA becomes negative-tone when exposed at a much higher electron dose (~20 000 μC cm^{-2}) which cross-links macromolecules and transforms the resist into higher-density graphitic nanostructures through a carbonization process [42, 43, 37]. Cross-linked PMMA has good solvent resistance and its atoms are connected by shorter-range carbon–carbon covalent bonds (bond lengths 120–154 pm) instead of van der Waals force between molecules as in normal PMMA [37], making it an effective screening mask impermeable to ions (~1 nm) in the electrolyte. Atomic force microscopy shows a continuous and smooth resist surface (root mean square surface roughness of 0.32 nm) without major defects or pinholes, indicating uniform dielectric thickness and promising high insulation (see supplementary information). Cyclic voltammetry (CV) measurements of graphene samples covered by masks of different thicknesses (illustrated in figure 2(b)) show strongly reduced charging current for mask-protected samples, as shown in the inset of figure 2(c). The subsequent calculation and model fitting of the capacitance of the electrolyte/PMMA-mask system (figure 2(c)) confirm that cross-linked PMMA is indeed largely impermeable to electrolyte, with an ion infiltration layer thickness of only 1.5 ± 3.4 nm (see

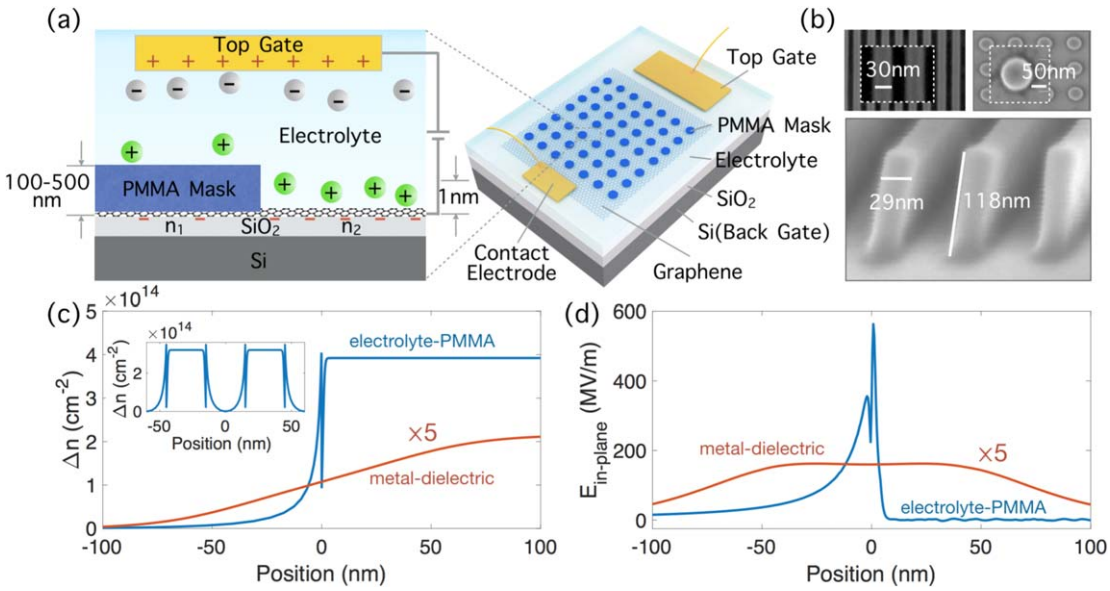

Figure 1. Nanopatterning of electrolyte gates. (a) Geometry and working principle of nanoscale electrolytic doping of 2D materials with a PMMA screening mask. n_1 and n_2 denote charge carrier densities in the mask-protected region and the exposed region, respectively. The charge carrier density contrast is defined as $\Delta n = |n_1 - n_2|$. (b) Scanning electron micrographs (SEMs) of example fabricated PMMA masks with nanoscale dimensions. (c) Simulated charge carrier density n profile for a single junction, compared between the proposed electrolyte-PMMA-mask gating scheme and a metal-dielectric split gating scheme. Inset: simulated charge carrier density n profile for the proposed electrolyte-PMMA gating scheme with a periodic PMMA mask with width $l = 30$ nm and thickness $d = 100$ nm. (d) Simulated in-plane electric field intensity $E_{\text{in-plane}}$ for a single junction, compared between the proposed electrolyte-PMMA-mask gating scheme and a metal-dielectric split gating scheme. Simulation parameters used in (c) and (d) are summarized below: the gate voltages are $V_{\text{tg}} = 15$ V for the electrolyte-PMMA gating scheme, and $V_{\text{lg}} = -60$ V and $V_{\text{rg}} = 60$ V for the metal-dielectric gating scheme. The dielectric gate has a thickness of 60 nm. The PMMA mask has a thickness of 100 nm. A gap of 100 nm is assumed between the two metal split gates. In the calculation of $E_{\text{in-plane}}$, an additional hexagonal boron nitride capping layer of 1 nm on top of the 2D material is included. Additional details on models and parameters used are in the supplementary information.

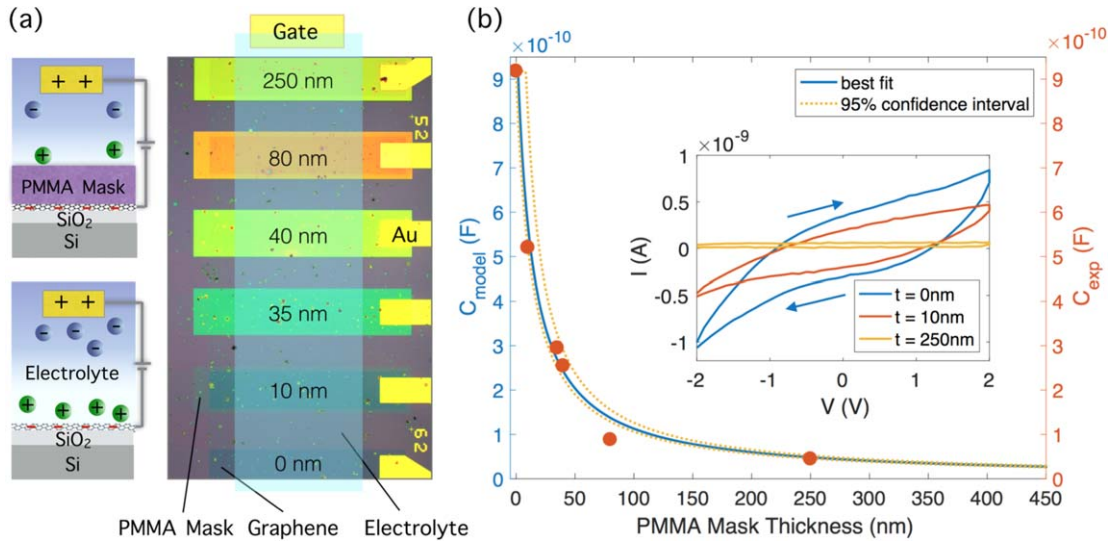

Figure 2. Cyclic voltammetry characterization of electrolyte-covered graphene samples protected by PMMA masks of different thicknesses: (a) measurement schematic diagrams for the cyclic voltammmetry (CV) characterization and an optical micrograph of the measured devices. An electrical voltage is applied between gate electrode and the graphene surface and ramped linearly with time from -2 to 2 V back and forth at a rate of 0.5 V s^{-1} for a few times. (c) Capacitance of the PMMA-mask/electrolyte system extracted from the CV measurements (red dots) and fitted to a simple model (blue curve) as a function of the mask thickness. The area between the two yellow dotted lines indicates the 95% confidence interval of the fitting. Inset: measured CV curves for samples with different PMMA mask thicknesses. The arrows indicate the voltage sweeping directions.

supplementary information for a detailed discussion of the model). In separate experiments, we use scanning-electron-microscopy to image the cross section of patterned cross-linked PMMA nanowires covered with electrolyte, verifying the eletrolyte's ability to wet and fill narrow slits of at least 20 nm and remain good contact

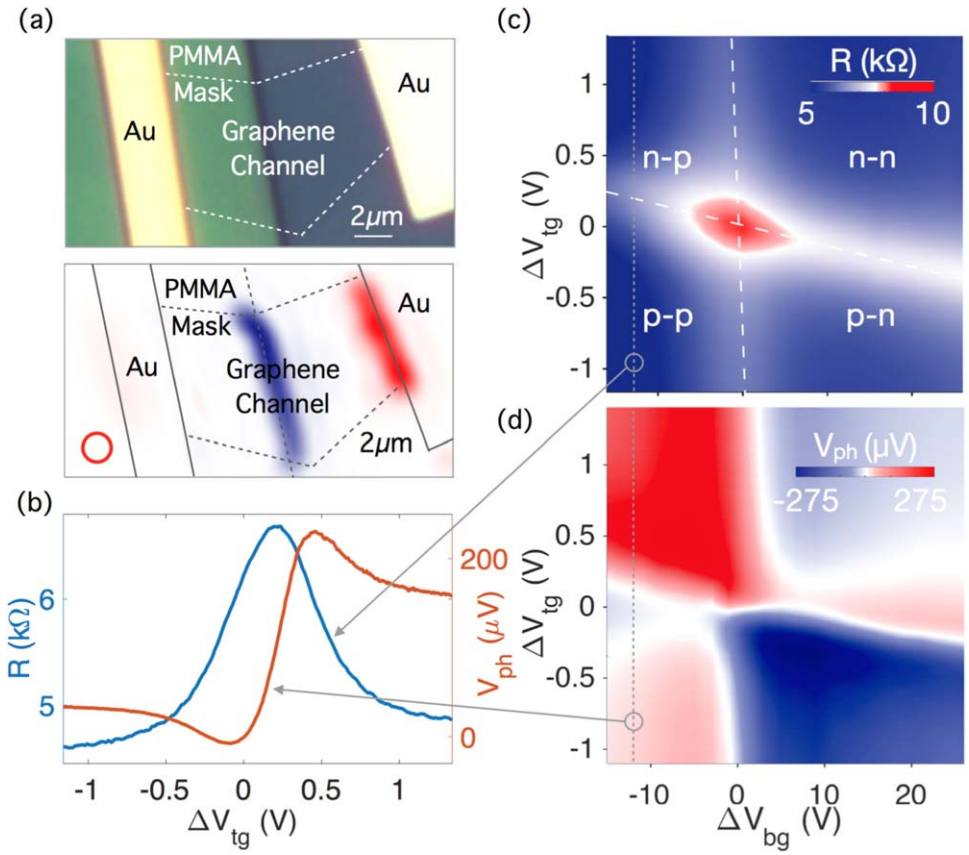

Figure 3. Gate-tunable graphene *p–n* junction and its photoresponse. (a) Top: optical image of the graphene *p–n* junction device before covering with the electrolyte. Half of the graphene channel is covered by a PMMA mask. Bottom: photovoltage V_{ph} spatial mapping of the *p–n* junction device conducted on a near-infrared ($\lambda = 1.55$ μm) confocal scanning microscopy setup. The red circle indicates the FWHM of the laser spot (~1.7 μm). (b) Resistance R and photovoltage V_{ph} as a function of V_{tg}, measured at $\Delta V_{bg} = -12$ V (line traces for (c) and (d) along the gray dotted line). (c) Resistance R as a function of V_{tg} and V_{bg}. White dashed lines indicate charge neutrality points of the top- and bottom-gated halves of the channel, and the four regions correspond to four doping configurations of the channel. (d) Photovoltage V_{ph} as a function of V_{tg} and V_{bg}, measured at the *p–n* interface.

with finely patterned nanostructures (see supplementary information). These experimental findings validate assumptions we made in the simulation and support the calculated results.

The spatial carrier density modulation resolution of the local electrolytic gates is determined by two factors: the e-beam lithography resolution of the screening mask and the sharpness of the junction. As shown in the simulation, the junction sharpness is ~15 nm, and the e-beam resolution has previously been demonstrated to be sub-10 nm [42], so the spatial modulation resolution using this technique is limited by roughly twice the junction sharpness, which is 30nm. The simulation in the inset of figure 1(c) indicates a well-defined carrier density modulation profile resulting from periodic local electrolyte gates with a half-pitch of 30 nm. Figure 1(b) shows SEM images of examples PMMA mask on graphene with this resolution and different geometries, including disks and ribbons. The cross section of the resist mask ribbons indicates straight sidewalls.

As proof-of-principle studies, we apply this technique to demonstrate the dynamical tuning of a graphene *p–n* junction. The device, shown in figure 3(a) (top panel), consists of a graphene channel covered in half by a PMMA mask. The graphene is exfoliated onto a 285 nm SiO_2 substrate thermally grown on doped Si. It is then patterned by e-beam lithography and reactive ion etching into a channel roughly 10 μm in length and 5 μm in width. A pair of Cr/Au contacts and a PMMA mask are then defined by e-beam lithography. Solid polymer electrolyte PEO−$LiClO_4$ is then drop-casted to cover the entire device.

Large-range doping level control of the two regions in a *p–n* junction can be achieved by tuning electrolyte top gate and SiO_2 back gate voltages, where V_{tg} controls the mask-uncovered region and V_{bg} mostly controls the mask-covered region. Figure 3(c) shows the channel resistance R versus V_{tg} and V_{bg}, showing four distinct characteristic regions that indicate gate-voltage-tunable charge density at a *p–n* interface [44]. Two intersecting lines of high resistance (white dashed), representing charge neutrality points of the two regions respectively, divide the resistance map into four low-resistance regions: *p–n*, *p–p*, *n–p*, and *n–n*. A vertical line trace of the 2D resistance map along the dotted gray line, shown in the blue curve of figure 3(b), exhibits distinct Dirac peak indicating modulation of graphene's Fermi level across the charge neutrality point.

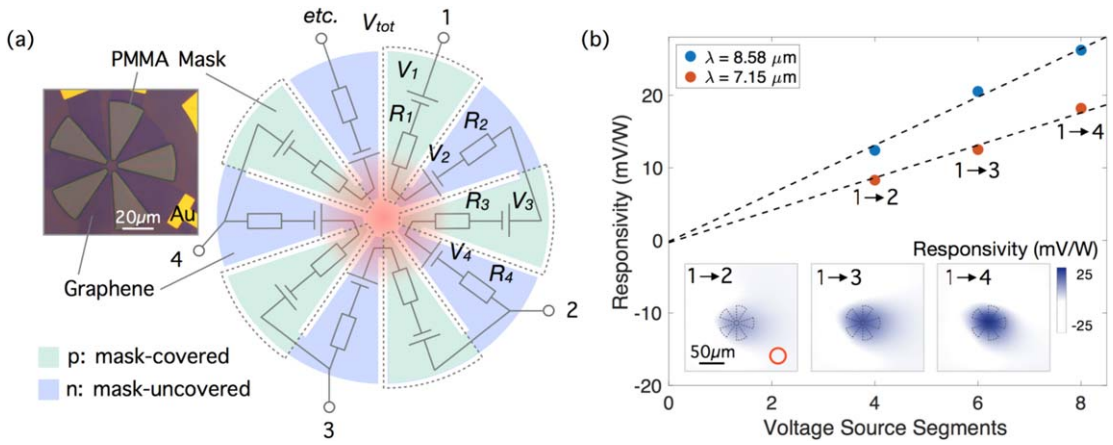

Figure 4. Compact graphene thermopile design and its photoresponse. (a) Equivalent circuit diagram and optical image of the graphene thermopile design. Graphene is etched into a circular channel with a meandering shape, with each segment acting as a voltage source and a serial resistance. The segments are *p*- or *n*-doped in an alternating way to produce photovoltage in the same direction along the channel. The doping pattern is generated by covering every other graphene segments with a PMMA mask and apply appropriate V_{tg} and V_{bg}. (b) Photovoltage responsivity of the thermopile measured at the center of the device as a function of the number of voltage source segments included in the circuit at $\lambda = 8.58$ μm and $\lambda = 7.15$ μm. Data points are fitted with a linear curve indicated by the dashed line. Inset: photovoltage responsivity spatial mappings of the thermopile measured at $\lambda = 8.58$ μm, with 4, 6 and 8 voltage source segments included in the circuit, respectively. The dashed circles indicate the size of the thermopile device. The red circle indicates the FWHM of the laser spot (~30 μm).

Photoresponse observed at the graphene *p*–*n* junction can also be dynamically tuned by the gate voltages. Figure 3(a) (bottom panel) shows the spatially-resolved open-circuit photovoltage map of the device under zero bias voltage across the channel, conducted on a near-infrared ($\lambda = 1.55$ μm) confocal scanning microscopy setup at room temperature. As the laser excitation is scanned over the device, a large photovoltage V_{ph} is observed at the electrolyte gate defined junction. This photovoltage V_{ph} at the junction as a function of V_{tg} and V_{bg}, plotted in figure 3(d), exhibits a distinct six-fold pattern with alternating photovoltage signs, showing a strong dependence of the photoresponse on the relative doping level of the graphene junction. This six-fold pattern indicates a photo-induced hot carrier-assisted photoresponse process at the graphene *p*–*n* junction known as the photo-thermoelectric (PTE) effect [45]. A vertical line trace of the 2D photovoltage map along the same dotted gray line, plotted in the red curve of figure 3(b), shows typical non-monotonic gate voltage dependence as a result of the PTE effect.

Leveraging the spatial gating versatility of this technique and the PTE effect in graphene, we design and demonstrate a compact mid-infrared graphene thermopile. The thermopile has 8 thermocouples connected in series and arranged in a geometry that optimizes voltage collection for free-space incident radiation with a Gaussian profile. The geometry flexibility of the patterned electrolyte gating technique eases the fabrication process and results in a small device footprint that is comparable to the diffraction limited beam size of mid-infrared light.

In this design a complex doping pattern of graphene is created to enhance the thermopile's photovoltage responsivity. For PTE effect, the photovoltage generated can be expressed as $V_{ph} = \int S(n, x)\Delta T(x)\mathrm{d}x$, where S is the Seebeck coefficient of graphene, a function of charge carrier density, and ΔT is the increase in electron temperature from the environment. For free-space incident light that has a spherical Gaussian profile, the temperature gradient points in the radial direction, so the photovoltage is maximized when it is collected radially.

The designed thermopile geometry, whose equivalent circuit diagram is illustrated in figure 4(a), consists of several thermocouples connected in series whose photovoltages are all collected in the radial direction. Each graphene segment is considered a voltage source with a resistance. For the photovoltage to sum up along the meandering graphene channel, each segment is *p*- or *n*-doped in an alternating fashion so that neighboring photovoltages point in opposite directions (Seebeck coefficient has opposite signs). The alternating doping is achieved using our gating technique by covering every other segments with the PMMA mask and applying positive V_{tg} and negative V_{bg} respectively. Compared to existing graphene thermopiles such as that in [46], this approach eliminates the need for embedded gates and external wiring of thermocouples, enabling a compact thermopile based solely on graphene.

Spatially-resolved open-circuit photovoltage mapping of this thermopile is conducted on a confocal scanning microscopy setup with a mid-infrared laser source at two wavelengths $\lambda = 8.58$ μm and $\lambda = 7.15$ μm. The photovoltage between several sets of terminals (indicated with numbers in figure 4(a)) are measured to study

the individual contributions of thermocouples. As the laser spot is scanned over the device, a maximal photovoltage V_{ph} is observed at the center of the thermopile, as shown in the photovoltage spatial maps in the inset of figure 4(b). The spatial maximum for responsivity is then plotted as a function of the number of voltage source segments between the terminals. The well-fitted linear relation at both wavelengths confirms the summation of photovoltages from each individual segment. The maximal responsivity of this device is 26.2 mV W^{-1} at $\lambda = 8.58$ μm, when 8 voltage segments are included in the device. Compared to a previous graphene thermocouple with only one single *p–n* junction, studied in similar conditions [47], the carefully designed doping pattern of graphene results in an about 7 times enhancement in photovoltage responsivity. Further optimization of parameters including device dimension and the number of voltage segments can be done to achieve higher responsivity (see supplementary information for a detailed discussion), and the device can be suspended as in [46] to benefit from higher temperature gradient as well.

4. Discussion

The flexibility to tailor the dimension and geometry of electrolyte gates on 2D materials at the nanoscale with strong doping ability expands the possibility of 2D-material-based tunable optoelectronic devices. The broadband optical transparency of the PMMA mask also ensures unaffected performance of optical designs such as waveguide and resonator modes and allows non-interfered optical spectroscopy. Moreover, although electrolyte and cross-linked PMMA can be sources of disorder that might degrade the quality of the gated material, when high sample mobility is desirable this limitation can be overcome by protecting the sample with a monolayer or few-layer hexagonal boron nitride before deposition of the electrolyte and the mask [48]. These are important practical considerations that can be crucial for the experimental implementation of many novel device concepts. Plasmonics in graphene would be an example. To achieve a plasmonic resonant wavelength of 5 μm or less, graphene nanostructures need to have a feature size as small as 30 nm combined with high carrier densities. This typically requires direct patterning of the graphene sheet, which on this small scale would create significant edge scattering and reduce carrier mobility, limiting the quality factor of the graphene plasmonic resonances [49]. The nanoscale electrolytic gating scheme proposed here would be an alternative and promising way of generating tunable graphene plasmons with an improved quality factor and a broader wavelength range.

5. Conclusion

To conclude, we have proposed and numerically simulated a nanopatterned electrolyte gating method of 2D materials that allows for a carrier density contrast of more than $\Delta n = 10^{14}$ cm^{-2} across a length of 15 nm and an in-plane electric field of 550 MV m^{-1}. We have developed an experimental implementation of this technique using cross-linked PMMA as the resist mask and verified its spatial patterning resolution of 30 nm, its impenetrability to electrolyte ions, the straightness of the mask sidewalls, and the ability for the electrolyte to fill, wet and maintain contact with finely patterned mask nanostructures. Taking advantage of the spatial versatility of this gating technique, we have designed and demonstrated a compact mid-infrared graphene thermopile whose geometry is optimized for free-space Gaussian incident radiation. The thermopile has a small footprint despite the number of thermocouples in the device that are connected in series, paving the way for more compact high-speed thermal detectors and cameras. This nanopatterned electrolytic gating scheme is a promising and versatile experimental approach to numerous 2D material-based device concepts in tunable nanophotonics and optoelectronics, and can potentially be used for other low-dimensional material classes too.

Acknowledgments

The research leading to these results has received funding from the US Office of Naval Research (Award N00014-14-1-0349), US Army Research Laboratory (Award W911NF-17-1-0435), the Center for Excitonics, an Energy Frontier Research Center funded by the US Department of Energy, Office of Science, Office of Basic Energy Sciences (Award no. DE-SC0001088), the European Commission H2020 Programme (no. 604391, 'Graphene Flagship'), the European Research Council starting grant (307806, CarbonLight) and project GRASP (FP7-ICT-2013-613024-GRASP). CP was supported in part by the Stata Family Presidential Fellowship of MIT, in part by the US Office of Naval Research (Award N00014-14-1-0349), and in part by the Center for Excitonics, an Energy Frontier Research Center funded by the US Department of Energy, Office of Science, Office of Basic Energy Sciences under award no. DE- SC0001088. DKE was supported in part by an Advanced Concept Committee (ACC) program from MIT Lincoln Laboratory. SN was supported by the European Commission (FP7-ICT-2013-613024-GRASP) and thanks M Batzer and R Parret for their help in exploratory work on this subject. R-JS

was supported in part by the Center for Excitonics, an Energy Frontier Research Center funded by the US Department of Energy, Office of Science, Office of Basic Energy Sciences under award no. DE-SC0001088. GG was supported by the Swiss National Science Foundation (SNSF). PJ-H and YY were supported in part by the US Department of Energy, Office of Basic Energy Sciences, Division of Materials Sciences and Engineering under award no. DE-SC0001819. Device fabrication was performed at the NanoStructures Laboratory at MIT and the Center for Nanoscale Systems, a member of the National Nanotechnology Infrastructure Network supported by the National Science Foundation (NSF).

ORCID iDs

Cheng Peng https://orcid.org/0000-0003-0308-3262

References

[1] Neamen D A 2003 *Semiconductor Physics and Devices* (New York: McGraw-Hill)
[2] Chuang S L 2012 *Physics of Photonic Devices* vol 80 (New York: Wiley)
[3] Ferrari A C *et al* 2015 Science and technology roadmap for graphene, related two-dimensional crystals, and hybrid systems *Nanoscale* **7** 4598–810
[4] Bao Q and Loh K P 2012 Graphene photonics, plasmonics, and broadband optoelectronic devices *ACS Nano* **6** 3677–94
[5] Avouris P and Freitag M 2014 Graphene photonics, plasmonics, and optoelectronics *IEEE J. Sel. Top. Quantum Electron.* **1** 6000112
[6] Koppens F H L, Mueller T, Avouris P, Ferrari A C, Vitiello M S and Polini M 2014 Photodetectors based on graphene, other two-dimensional materials and hybrid systems *Nat. Nanotechnol.* **9** 780–93
[7] Wang Q H, Kalantar-Zadeh K, Kis A, Coleman J N and Strano M S 2012 Electronics and optoelectronics of two-dimensional transition metal dichalcogenides *Nat. Nanotechnol.* **7** 699–712
[8] Britnell L *et al* 2013 Strong light–matter interactions in heterostructures of atomically thin films *Science* **340** 1311–4
[9] Liu C-H, Chang Y-C, Norris T B and Zhong Z 2014 Graphene photodetectors with ultra-broadband and high responsivity at room temperature *Nat. Nanotechnol.* **9** 273–8
[10] Sassi U *et al* 2017 Graphene-based mid-infrared room-temperature pyroelectric bolometers with ultrahigh temperature coefficient of resistance *Nat. Commun.* **8** 14311
[11] Roy T, Tosun M, Cao X, Fang H, Lien D-H, Zhao P, Chen Y-Z, Chueh Y-L, Guo J and Javey A 2015 Dual-gated MoS_2/WSe_2 van der waals tunnel diodes and transistors *Acs Nano* **9** 2071–9
[12] Cheianov V V, Fal'ko V and Altshuler B L 2007 The focusing of electron flow and a veselago lens in graphene pn junctions *Science* **315** 1252–5
[13] Shang X J, He J F, Wang H L, Li M F, Zhu Y, Niu Z C and Fu Y 2011 Effect of built-in electric field in photovoltaic inas quantum dot embedded gaas solar cell *Appl. Phys.* A **103** 335–41
[14] Konstantatos G and Sargent E H 2010 Nanostructured materials for photon detection *Nat. Nanotechnol.* **5** 391–400
[15] Thongrattanasiri S, Koppens F H L and de Abajo F J 2012 Complete optical absorption in periodically patterned graphene *Phys. Rev. Lett.* **108** 047401
[16] Ye C, Zhu Z, Xu W, Yuan X and Qin S 2015 Electrically tunable absorber based on nonstructured graphene *J. Opt.* **17** 125009
[17] Vakil A and Engheta N 2011 Transformation optics using graphene *Science* **332** 1291–4
[18] Yankowitz M, Xue J, Cormode D, Sanchez-Yamagishi J D, Watanabe K, Taniguchi T, Jarillo-Herrero P, Jacquod P and LeRoy B J 2012 Emergence of superlattice dirac points in graphene on hexagonal boron nitride *Nat. Phys.* **8** 382–6
[19] Kang J, Li J, Li S-S, Xia J-B and Wang L-W 2013 Electronic structural moire pattern effects on $MoS_2/MoSe_2$ 2d heterostructures *Nano Lett.* **13** 5485–90
[20] Park C-H, Yang L, Son Y-W, Cohen M L and Louie S G 2008 Anisotropic behaviours of massless dirac fermions in graphene under periodic potentials *Nat. Phys.* **4** 213–7
[21] Park C-H, Son Y-W, Yang L, Cohen M L and Louie S G 2008 Electron beam supercollimation in graphene superlattices *Nano Lett.* **8** 2920–4
[22] Baugher B W H, Churchill H O H, Yang Y and Jarillo-Herrero P 2014 Optoelectronic devices based on electrically tunable pn diodes in a monolayer dichalcogenide *Nat. Nanotechnol.* **9** 262–7
[23] Pospischil A, Furchi M M and Mueller T 2014 Solar-energy conversion and light emission in an atomic monolayer pn diode *Nat. Nanotechnol.* **9** 257–61
[24] Ross J S *et al* 2014 Electrically tunable excitonic light-emitting diodes based on monolayer WSe_2 p–n junctions *Nat. Nanotechnol.* **9** 268–72
[25] Novoselov K S, Geim A K, Morozov S V, Jiang D, Zhang Y_, Dubonos S V, Grigorieva I V and Firsov A A 2004 Electric field effect in atomically thin carbon films *Science* **306** 666–9
[26] McPherson J, Kim J-Y, Shanware A and Mogul H 2003 Thermochemical description of dielectric breakdown in high dielectric constant materials *Appl. Phys. Lett.* **82** 2121
[27] Sire C, Blonkowski S, Gordon M J and Baron T 2007 Statistics of electrical breakdown field in HfO_2 and SiO_2 films from millimeter to nanometer length scales *Appl. Phys. Lett.* **91** 2905
[28] Hattori Y, Taniguchi T, Watanabe K and Nagashio K 2014 Layer-by-layer dielectric breakdown of hexagonal boron nitride *ACS Nano* **9** 916–21
[29] Efetov D K and Kim P 2010 Controlling electron–phonon interactions in graphene at ultrahigh carrier densities *Phys. Rev. Lett.* **105** 256805
[30] Ueno K, Nakamura S, Shimotani H, Yuan H T, Kimura N, Nojima T, Aoki H, Iwasa Y and Kawasaki M 2011 Discovery of superconductivity in $KTaO_3$ by electrostatic carrier doping *Nat. Nanotechnol.* **6** 408–12
[31] Ohno Y, Maehashi K, Yamashiro Y and Matsumoto K 2009 Electrolyte-gated graphene field-effect transistors for detecting ph and protein adsorption *Nano Lett.* **9** 3318–22

[32] Henriksen E A, Nandi D and Eisenstein J P 2012 Quantum hall effect and semimetallic behavior of dual-gated aba-stacked trilayer graphene *Phys. Rev.* X **2** 011004
[33] Hess L H, Hauf M V, Seifert M, Speck F, Seyller T, Stutzmann M, Sharp I D and Garrido J A 2011 High-transconductance graphene solution-gated field effect transistors *Appl. Phys. Lett.* **99** 033503
[34] Froehlicher G and Berciaud S 2015 Raman spectroscopy of electrochemically gated graphene transistors: geometrical capacitance, electron–phonon, electron–electron, and electron-defect scattering *Phys. Rev.* B **91** 205413
[35] Grover S, Joshi A, Tulapurkar A and Deshmukh M M 2017 Abrupt pn junction using ionic gating at zero-bias in bilayer graphene *Sci. Rep.* **7** 3336
[36] Bilenberg B, Jacobsen S, Schmidt M S, Skjolding L H D, Shi P, Bøggild P, Tegenfeldt J O and Kristensen A 2006 High resolution 100 kv electron beam lithography in su-8 *Microelectron. Eng.* **83** 1609–12
[37] Duan H, Zhao J, Zhang Y, Xie E and Han L 2009 Preparing patterned carbonaceous nanostructures directly by overexposure of pmma using electron-beam lithography *Nanotechnology* **20** 135306
[38] Comsol Inc 2015 *COMSOL MultiphysicsReference Manual: Version 5.0*(www.comsol.com)
[39] Bard A J, Faulkner L R, Leddy J and Zoski C G 1980 *Electrochemical Methods: Fundamentals and Applications* vol 2 (New York: Wiley)
[40] Chen W and Ahmed H 1993 Fabrication of 5–7 nm wide etched lines in silicon using 100 kev electron-beam lithography and polymethylmethacrylate resist *Appl. Phys. Lett.* **62** 1499–501
[41] Beaumont S P, Bower P G, Tamamura T and Wilkinson C D W 1981 Sub-20-nm-wide metal lines by electron-beam exposure of thin poly (methyl methacrylate) films and liftoff *Appl. Phys. Lett.* **38** 436–9
[42] Duan H, Winston D, Yang J K W, Cord B M, Manfrinato V R and Berggren K K 2010 Sub-10-nm half-pitch electron-beam lithography by using poly (methyl methacrylate) as a negative resist *J. Vac. Sci. Technol.* B **28** C6C58–62
[43] Duan H G, Xie E Q and Han L 2008 Turning electrospun poly (methyl methacrylate) nanofibers into graphitic nanostructures by *in situ* electron beam irradiation *J. Appl. Phys.* **103** 046105
[44] Williams J R, DiCarlo L and Marcus C M 2007 Quantum hall effect in a gate-controlled pn junction of graphene *Science* **317** 638–41
[45] Song J C W, Rudner M S, Marcus C M and Levitov L S 2011 Hot carrier transport and photocurrent response in graphene *Nano Lett.* **11** 4688–92
[46] Hsu A L *et al* 2015 Graphene-based thermopile for thermal imaging applications *Nano Lett.* **15** 7211–6
[47] Herring P K, Hsu A L, Gabor N M, Shin Y C, Kong J, Palacios T and Jarillo-Herrero P 2014 Photoresponse of an electrically tunable ambipolar graphene infrared thermocouple *Nano Lett.* **14** 901–7
[48] Gallagher P, Lee M, Petach T A, Stanwyck S W, Williams J R, Watanabe K, Taniguchi T and Goldhaber-Gordon D 2015 A high-mobility electronic system at an electrolyte-gated oxide surface *Nat. Commun.* **6** 6437
[49] Low T and Avouris P 2014 Graphene plasmonics for terahertz to mid-infrared applications *ACS Nano* **8** 1086–101